



# Electron redistribution of ruthenium-tungsten oxides Mott-Schottky heterojunction for enhanced hydrogen evolution

Lingxin Peng<sup>a,c,1</sup>, Liang Su<sup>b,1</sup>, Xu Yu<sup>a,c,1</sup>, Rongyan Wang<sup>a</sup>, Xiangzhi Cui<sup>a,c,d,\*</sup>, Han Tian<sup>a</sup>, Shaowen Cao<sup>e</sup>, Bao Yu Xia<sup>b,\*\*</sup>, Jianlin Shi<sup>a,c,\*</sup>

<sup>a</sup> State Key Laboratory of High Performance Ceramics and Superfine Microstructure, Shanghai Institute of Ceramics, Chinese Academy of Sciences, Shanghai 200050, China

<sup>b</sup> Key Laboratory of Material Chemistry for Energy Conversion and Storage (Ministry of Education), Hubei Key Laboratory of Material Chemistry and Service Failure, School of Chemistry and Chemical Engineering, Wuhan National Laboratory for Optoelectronics, Huazhong University of Science and Technology, 1037 Luoyu Road, Wuhan 430074, China

<sup>c</sup> Center of Materials Science and Optoelectronics Engineering, University of Chinese Academy of Sciences, Beijing 100049, China

<sup>d</sup> School of Chemistry and Materials Science, Hangzhou Institute for Advanced Study, University of Chinese Academy of Sciences, Hangzhou 310024, China

<sup>e</sup> State Key Laboratory of Advanced Technology for Materials Synthesis and Processing, Wuhan University of Technology, Wuhan 430070, China

## ARTICLE INFO

### Keywords:

Hydrogen evolution  
Surface engineering  
Mott-Schottky effect  
Electron redistribution

## ABSTRACT

Developing efficient electrocatalysts is of significance for hydrogen production in acid electrolyte. In this work, we report a facile decoration of ruthenium species onto tungsten oxides to construct the Mott-Schottky heterojunction electrocatalyst for hydrogen evolution. The resultant Ru-WO<sub>2.72</sub> hybrid exhibits a superior Ru-based mass activity of 161.6 times higher than that of commercial Ru/C for hydrogen evolution, featuring a Tafel slope of 50 mV dec<sup>-1</sup> and 40 mV overpotential at the current density of 10 mA cm<sup>-2</sup>. The uniform distribution of Ru species triggers a strong electron transfer across the Ru-WO<sub>2.72</sub> Schottky barrier, resulting in a largely increased local electron density on the active Ru surface. Such electron enrichment induced by the Mott-Schottky effect at the metal-metal oxides interface is responsible for enhanced hydrogen production. This work demonstrates an effective strategy by Mott-Schottky effect to regulate electron distribution, which would evoke more inspiration in designing efficient electrocatalysis and beyond.

## 1. Introduction

Electrochemical water splitting is one of environmental-friendly and significant approaches to support hydrogen energy and economics [1–3]. Proton exchange membrane (PEM) electrolyzer has a wide usage in hydrogen production, thus developing efficient and stable electrocatalyst is of great importance for the hydrogen evolution reaction (HER) in PEM electrolyzer with acidic medium [4]. To date, Pt-based materials are still commonly used in PEM electrolyzer due to their high catalytic activity [5]. However, their nature in high cost and scarcity greatly hinders the scale-up application for HER in PEM electrolyzer [6,7]. To tackle this dilemma, numerous efforts have been made to explore non-Pt substitutes for efficient and stable HER [8–10].

The electronic structure of electrocatalysts is one of the most important factors to determine its activities [11–13]. Defect engineering, including surface distortions and inner defects, is promising to modulate the local electron density [14–16], while heteroatom incorporation or substitution would be another effective strategy to regulate the electron distribution for promoting HER performance [17,18]. However, those approaches may lead to irreversible destruction of the crystal structure, resulting in the metastability and subsequent stability deterioration of the catalysts [19]. Consequently, developing novel concepts for no-damaged and low-cost electrocatalysts is of great significance yet challenging for HER in PEM electrolyzers. Mott-Schottky effect is a classic method to regulate the distribution of electrons in semiconductor devices [20]. The electron distribution can be regulated

\* Corresponding authors at: State Key Laboratory of High Performance Ceramics and Superfine Microstructure, Shanghai Institute of Ceramics, Chinese Academy of Sciences, Shanghai 200050, China.

\*\* Corresponding author.

E-mail addresses: [cuixz@mail.sic.ac.cn](mailto:cuixz@mail.sic.ac.cn) (X. Cui), [byxia@hust.edu.cn](mailto:byxia@hust.edu.cn) (B.Y. Xia), [jishi@mail.sic.ac.cn](mailto:jishi@mail.sic.ac.cn) (J. Shi).

<sup>1</sup> These authors contribute equally to this work.

by establishing a well-defined hybrid structure through Mott-Schottky heterojunction. Due to the differences of work functions between metal and metal oxide, the Fermi energy level will be bent to achieve a unity, which would trigger the directional transfer of electrons and form a barrier at the interface, thus realizing the electron rearrangement [21, 22]. The resultant enrichment of excessive electrons on the metal surface would facilitate the activation of hydrogen intermediates and accelerate the HER process [8,12].

Here, we report a facile construction of Ru-WO<sub>2.72</sub> Mott-Schottky heterojunction for efficient HER in acid solution. Tungsten oxide (WO<sub>3</sub>) is a typical material that can stably exist in acidic electrolyte, especially through the insertion/removal of hydrogen, it can form a hydrogen tungsten bronze compound (H<sub>y</sub>WO<sub>3</sub>) in acidic electrolyte, which would realize the transfer of hydrogen from WO<sub>3</sub> substrate to the active site, leading to the enhanced acidic HER [23,24]. Meanwhile, ruthenium (Ru), as a member of the Pt group metal, has excellent HER catalytic activity [25–27]. As WO<sub>2.72</sub> is a kind of non-stoichiometric tungsten oxide with strong surface species adsorption capability and weak reducibility, its preparation process is realized by its spontaneous reduction and formation of the low amount Ru species on the WO<sub>2.72</sub> nanowires, without any foreign reductive agents or stabilizing molecules. The as-obtained heterojunction hybrid with a low amount Ru loading (2.73 wt%) exhibits remarkable HER performance with a low overpotential of 40 mV at a current density of 10 mA cm<sup>-2</sup>, which is far better than that of commercial Ru/C and comparable to that of commercial Pt/C. Experimental analysis combined with density-functional-theory (DFT) calculations reveal that the electron redistribution at the metal-metal oxide interface induced by the Mott-Schottky heterojunction are synergistically responsible for the high electrocatalytic activity. This work not only provides a highly efficient HER electrocatalyst in acidic electrolyte but also demonstrates a facile and effective strategy in the electron regulation by constructing Mott-Schottky heterojunction, which would bring more enlightenment in design and preparation of advanced electrocatalysis for energy technologies.

## 2. Experimental section

### 2.1. Chemicals and materials

Tungsten (VI) chloride, ethanol, ruthenium trichloride, concentrated sulfuric acid, Commercial Pt/C (20 wt%), Ru/C (5 wt%) and all chemicals involved were all purchased from Aladdin. Nafion solution (5 wt%) was obtained from Sigma-Aldrich. All chemical reagents were used without any further purification.

### 2.2. Preparation of WO<sub>2.72</sub> nanowires

400 mg of tungsten (VI) chloride was dispersed in 80 mL of ethanol with the assistance of magnetic stirring. After stirring 0.5 h, the mixture was transferred into a 100 mL Teflon-lined stainless-steel autoclave. The vessel was sealed and heated at 160 °C for 10 h, and then cooled to room temperature naturally. The products were collected and purified by ethanol several times and evaporated at 60 °C for 24 h to get a dried powder.

### 2.3. Preparation of Ru-WO<sub>2.72</sub>

50 mg WO<sub>2.72</sub> powders were dissolved into 100 mL deionized water under continuous magnetic stirring. After stirring 1 h, a solution with 5 g L<sup>-1</sup> ruthenium trichloride was dropped slowly with the rate of 5 μL s<sup>-1</sup> under strong magnetic stirring. The formed samples were named as WR, WR1, WR2, and WR3 according to the addition of ruthenium trichloride solution of 1 mL, 0.1 mL, 0.5 mL, and 1.5 mL, respectively. The products were washed by water and ethanol several times, then the Ru-WO<sub>2.72</sub> composites were finally obtained after evaporated at 60 °C for 24 h.

### 2.4. Materials characterization

X-ray diffraction measurements were performed on a Rigaku D/Max 2200PC XRD system using Cu Kα radiation at 40 mA and 40 kV. Raman spectrum was collected by a Renishaw in-Via Raman microprobe equipped with a Leica DM 2500 M microscope system and 523 nm diode-pumped laser at a resolution of 4 cm<sup>-1</sup> in the range between 100 and 4000 cm<sup>-1</sup>. Transmission (TEM) electron microscopic images and energy-dispersive X-ray spectrometry (EDS) elemental mapping were performed on a JEOL 200CX electron microscope under 200 kV. Scanning Electron Microscope (SEM) images were obtained on FEI Magellan 400 instrument. X-ray photoelectron spectroscopy (XPS) measurement was conducted out on Thermo Scientific ESCALAB 250 spectrometer with Al Kα radiation as the excitation source. The spectra were calibrated by setting C 1 s to 284.6 eV. Electron spin resonance (ESR) signals were measured on a JEOL-FA200 ESR instrument. Photoluminescence spectrum (PL) were measured on a FluoroLog3–21 spectrofluorometer (HORIBA Jobin Yvon, France) with the excitation light at 325 nm. Ultraviolet photoemission spectroscopy (UPS) was also carried out on an ESCALAB 250 Xi spectrometer using He (I) resonance lines (21.2 eV). Inductively coupled plasma optical emission spectrometer (ICP-OES) was determined on Varian 720-ES. The X-ray absorption fine structure (XAFS) spectra at W L<sub>3</sub>-edge was performed at BL14W1 beamline of Shanghai Synchrotron Radiation Facility (SSRF). The XAFS data were recorded under transmission mode with ion chambers. The energy was calibrated accordingly to the absorption edge of pure Ta foil.

### 2.5. Electrochemical measurements

For the preparation of working electrodes, 5.0 mg of WR powders and 20 μL of Nafion (5 wt%) were dispersed in 1 mL of ethanol and water (1:1 in volume). The mixture was ultrasonicated for at least 30 min to generate a homogeneous ink, then 10 μL of ink was dropped onto the glassy carbon electrode with a diameter of 5 mm. The amount of catalyst deposited on the glassy carbon electrode was controlled as 0.25 mg cm<sup>-2</sup>. All electrochemical measurement was performed at room temperature by using a CHI 760E electrochemical workstation (CH Instrument, Shanghai, China) with a standard three-electrode cell. An Ag/AgCl in 3 M KCl solution acted as the reference electrode, and a graphite rod (6 mm in diameter) was used as counter electrode. An aqueous solution of 0.5 M H<sub>2</sub>SO<sub>4</sub> was used as the electrolyte. All potentials were referenced to a reversible hydrogen electrode (RHE) with 90% iR correction:  $E_{vs\ RHE} = E_{vs\ Ag/AgCl} + 0.0591 \cdot pH + E_{Ag/AgCl}^0 (0.209) - iR$ , where the R was referred to the average ohmic resistance obtained from EIS measurement. The scan rate of cyclic voltammetry (CV) is 0.05 V s<sup>-1</sup>, while that is 0.005 V s<sup>-1</sup> for linear sweep voltammetry (LSV). Electrochemical impedance spectroscopy (EIS) was performed from 100 KHz to 0.01 Hz at 50 mV (vs RHE) with an amplitude of 5 mV. Cyclic voltammetry (CV) was conducted to measure the electrochemical double layer capacitance (EDLC) at non-Faradaic potential ranging from 0.1 to 0.2 V (vs. RHE) with various scan rates (20, 40, 60, 80, 100 mV s<sup>-1</sup>), which can estimate the effective electrochemical surface area. The long-time stability of catalysts was also tested by chronoamperometry, which was carried out at constant overpotential of 50 mV for 10 h. A flow of N<sub>2</sub> was maintained during the experiment. Faradaic efficiencies were calculated via the H<sub>2</sub> production rate, which was detected by a chromatography system S3(GC 2030plus, Tet) at a constant current density of 10 mA cm<sup>-2</sup>. Theoretical H<sub>2</sub> volume was obtained based on Faradaic's law of electrolysis. MS curves were plotted with a fixed frequency of 750 Hz.

### 2.6. Electrochemical evaluation (*b*, *j*<sub>0</sub>, *C*<sub>dl</sub>, ESCA, TOF)

Tafel slope (*b*) and exchange current density (*j*<sub>0</sub>): Tafel plots can be obtained by fitting the polarization curves as overpotential versus log current density:  $\eta = a + b \log[j]$ ,  $\eta$  is overpotential,  $j$  is current density

and  $b$  is Tafel slope, which obtained by fitting in the linear region of Tafel curve and used to indicate the characteristics of the hydrogen evolution reaction kinetics. Exchange current density ( $j_0$ ) is the intersection of the Tafel curve in the extension in linear region, which also reveals the kinetics of hydrogen evolution reaction and the intrinsic activity of electrocatalysts. Electrochemical double layer capacitance ( $C_{dl}$ ) and electrochemical active surface area (ECSA) were evaluated by cyclic voltammetry in non-Faradaic region at various scan rates, and the capacitive current density ( $|j_a - j_c|/2$ ) is proportional to the scan rate ( $\nu$ ). Moreover, the electrochemical active surface area is calculated from the electrochemical double layer capacitance:  $S_{ECSA} = C_{dl}/C_s$ , where  $C_s$  is the specific capacitance of the material or the capacitance of an atomically smooth planar surface of the material per unit area under identical electrolyte conditions, here, we adopt general specific capacitances of  $C_s = 0.04 \text{ mF cm}^{-2}$ . The turnover frequency (TOF) was calculated according to the equation:  $\text{TOF} = \frac{j_s}{2nF}$ , Where  $j$  is the current density at an overpotential of 100 mV,  $S$  is the geometric surface area of GC electrode

( $0.196 \text{ cm}^2$ ), 2 stands for a two electron reaction process in HER,  $F$  is Faraday constant ( $96,500 \text{ C/mol}$ ),  $n$  is the number of moles of metal atoms deposited onto the GC electrodes that calculated from mass loading.

## 2.7. Calculation methods

The calculations of geometry optimization, work function and electron density of state were carried out by density functional theory (DFT) as implemented in the Vienna ab initio simulation package code (VASP version 5.3.3) [28], using a plane wave basis set with the projector augmented wave (PAW) pseudopotential for the inner electrons [29], and the generalized gradient approximation (GGA) in the form of Perdew-Burke-Ernzerhof (PBE) for the exchange-correlation potentials [30]. A kinetic cutoff energy of 560 eV for the valence electrons was set and the atomic positions were allowed to relax in the configurations for three directions until the force and energy on each atom were smaller

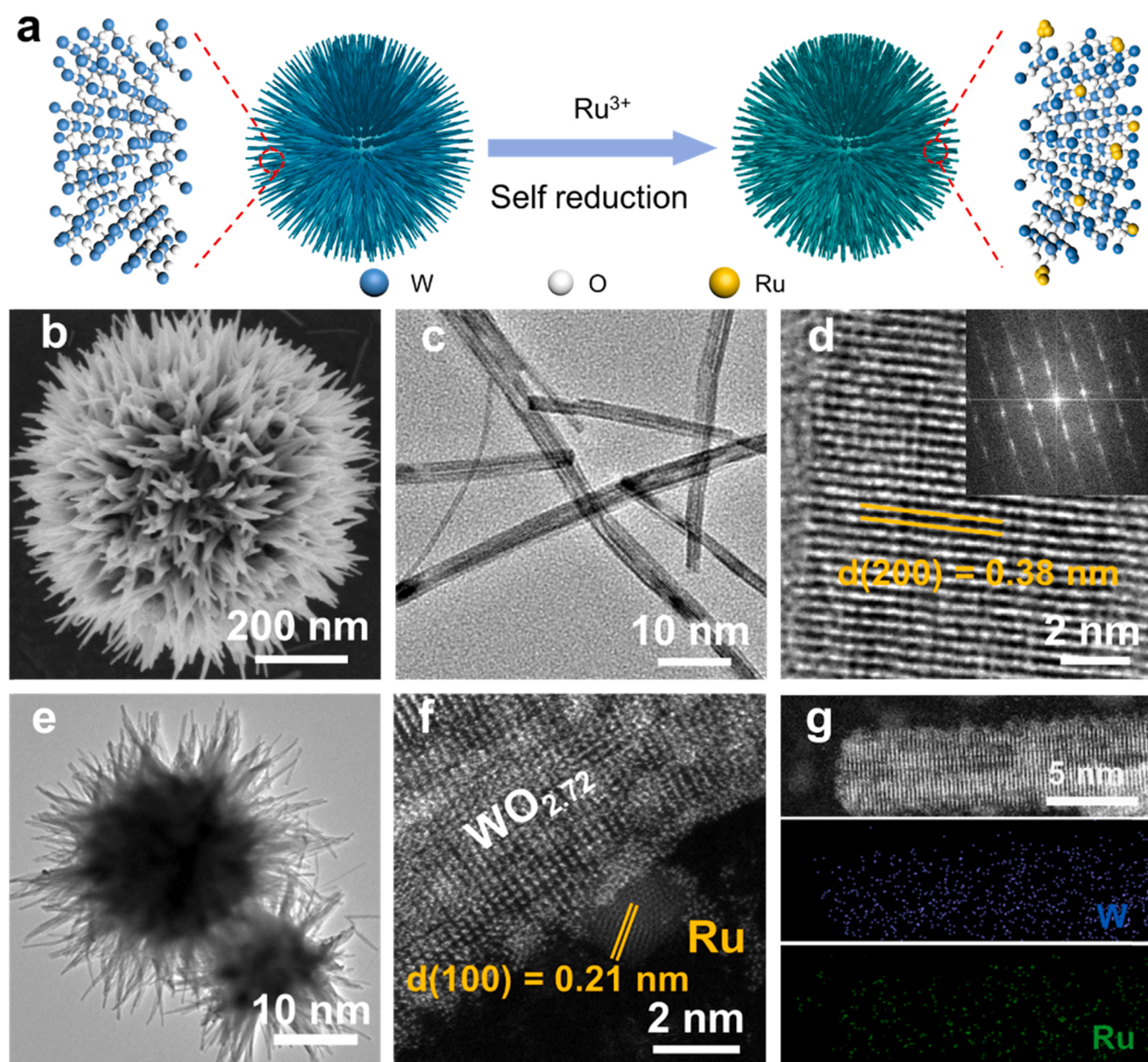


**Fig. 1.** (a) Schematic synthesis of WR heterojunction, (b) SEM, (c) TEM, and (d) HRTEM images of  $\text{WO}_{2.72}$ . Inset d is the corresponding FFT pattern. (e) TEM, (f) HRTEM and (g) HAADF-STEM and elemental mapping images of WR composite.



than  $0.01 \text{ eV } \text{\AA}^{-1}$  and  $10^{-4} \text{ eV}$ , respectively. The model of  $\text{WO}_{2.72}$  nanowires surface ( $17.836 \text{ \AA} \times 17.836 \text{ \AA}$ ) were constructed with 4–9 layers. Finally, a four-layer slab was test and chosen to model  $\text{WO}_{2.72}$  surface. The cluster of Ru metal atom with  $\text{WO}_{2.72}$  surface was simulated with Ru bonding to two O atoms in  $\text{WO}_{2.72}$ . In each case, a vacuum space of  $\sim 15 \text{ \AA}$  along the Z direction was applied to prevent unphysical interaction between the neighboring slabs. The top two layers in the model of Ru cluster combined with  $\text{WO}_{2.72}$  surface was relaxed during optimization, while the remaining layers were fixed to mimic the bulk. For the calculation of density of states (DOS), the  $k$ -mesh was chosen to  $3 \times 4 \times 1$  for calculation of the surface sample Brillouin-zone. The work function (WF) of model that Ru combined with  $\text{WO}_{2.72}$  surface was also calculated, which dependent on the position of the Fermi level. The free energy calculation of hydrogen adsorption ( $\Delta G_{\text{H}^*}$ ) is based on Nørskovetals' hydrogen electrode model, which was defined as follows:

$$\Delta G_{\text{H}^*} = \Delta E_{\text{H}^*} + \Delta E_{\text{ZPE}} - T\Delta S$$

Where  $\Delta E$ ,  $\Delta E_{\text{ZPE}}$ , and  $\Delta S$  respectively represent the changes of electronic energy, zero-point energy, and entropy that caused by adsorption of hydrogen. The ideal hydrogen adsorption free energy value ( $\Delta G_{\text{H}^*}$ ) is near zero, which could balance the adsorption and desorption of hydrogen reaction.

### 3. Results and discussion

#### 3.1. Catalyst synthesis and characterization

The formation of Ru- $\text{WO}_{2.72}$  (WR) Mott-Schottky heterojunction is realized by reducing and decorating low amount Ru species onto the  $\text{WO}_{2.72}$  substrate, as illustrated in Fig. 1a. In this process, the moderately reductive  $\text{WO}_{2.72}$  is the key to realize the reduction and deposition of Ru species. Scanning electron microscopy (SEM) images show the flower-like spheres obtained by a solvothermal method (Fig. 1b), which are composed of radial  $\text{WO}_{2.72}$  nanowires (Fig. 1c). High-resolution transmission electron microscopy (HRTEM) demonstrates the well-resolved lattice fringes of  $0.38 \text{ nm}$ , being attributed to the (010) plane of monoclinic  $\text{WO}_{2.72}$  (Fig. 1d). The fast Fourier transformation (FFT) pattern further confirms the single crystalline nature of  $\text{WO}_{2.72}$  (Fig. 1d inset) [31]. Their crystalline information is further verified by X-ray diffraction (XRD) analysis (Fig. S1a). Two main diffraction peaks at  $23^\circ$  and  $48^\circ$  are assigned to the (010) and (020) planes of monoclinic  $\text{W}_{18}\text{O}_{49}$  consisting of the edge-sharing distorted  $\text{WO}_6$  octahedron (PDF: 05-0392, Fig. S1b) [31,32], which is different from the cube  $\text{WO}_3$  phase (Fig. S1c) [33]. While the WR composite remains the similar XRD profile (Fig. S1a), suggesting no distinctive changes even after the decoration of Ru species. Moreover, the character of Ru crystalline is also absent, which means the small amount Ru may be present in the smaller size even atomically dispersed on the  $\text{WO}_{2.72}$ . Transmission electron microscopy (TEM) observation further verifies the retained initial sphere morphology composed of abundant radial nanowires (Fig. 1e). HRTEM image in Fig. 1f validates the presence of Ru species (less than  $2 \text{ nm}$ ), and these clusters are closely anchored on the surface of  $\text{WO}_{2.72}$  nanowires, which evidencing the successful reduction and decoration of Ru species on  $\text{WO}_{2.72}$  nanowires by self-redox reaction without any other reductive agents involved. Moreover, high-angle annular dark-field scanning transmission electron microscopy (HAADF-STEM) image in Fig. 1g clearly reveals the attachment of atomically scattered Ru clusters. The Ru loading of  $\sim 2.73 \text{ wt\%}$  is estimated by the energy dispersive X-ray spectroscopy (EDS) (Fig. S2) and verified by the inductively-coupled-plasma optical emission spectrometer (ICP-OES) (Table S1). In addition, the SEM and TEM images of WR1, WR2, WR3 samples are shown in Fig. S3, Fig. S4, and Fig. S5, respectively, and the morphology of urchin-like nanosphere can be maintained. While the nanowires of the WR3 are much shorter compare to other samples due to the increasement of Ru loading (Fig. S5), which may result in the

decrease of the active site exposure.

The formation of WR heterojunction is further investigated by Raman spectra (Fig. S6). Except for the typical vibration modes of O-W-O and W-O in  $\text{WO}_{2.72}$  and WR, a Ru-O-W vibration is found at  $\sim 400 \text{ cm}^{-1}$  for the WR sample [31]. Meanwhile, the X-ray photoelectron spectra (XPS) of  $\text{WO}_{2.72}$  and WR show a typical pair of W  $4f_{5/2}$  and W  $4f_{7/2}$  (Fig. 2a). Two main peaks at  $36.3$  and  $38.2 \text{ eV}$  are assigned to W  $4f_{5/2}$  of W (VI), while the peak at  $34.7 \text{ eV}$  corresponds to W(V) [34]. The co-existence of W(VI) and W(V) species is attributed to the corner-sharing and edge-sharing W sites in the  $[\text{WO}_6]$  octahedron [35]. The proportion of W(V) in WR sample decreased substantially compared with  $\text{WO}_{2.72}$  sample (Table S2), indicating W acts as an electron provider. Moreover, The O 1s XPS spectra can be resolved into three peaks (Fig. S7a), and the peaks at  $530.5 \text{ eV}$  and  $531.7 \text{ eV}$  are attributed to the lattice oxygen and surface oxygen species, respectively, while the peak at  $532.4 \text{ eV}$  is corresponding to the oxygen vacancy [36,37]. Meanwhile, after the loading of Ru, the proportions of the oxygen species did not change significantly (Figs. S7–S10, Table S3). The result of electron spin resonance (ESR) spectra (Fig. S11) shows a signal at  $g = 2.02$ , which evidences the presence of oxygen defects in the  $\text{WO}_{2.72}$  and WR samples (Fig. S7a) [38]. Moreover, no significant difference is observed in the ESR intensity between the  $\text{WO}_{2.72}$  and WR samples, indicating the negligible influence of Ru species on oxygen vacancies. Furthermore, the Ru 3d XPS signal displays two evident peaks at  $280.6$  and  $282.05 \text{ eV}$  assigned to Ru  $3d_{5/2}$ , in addition to the peak at  $284.8 \text{ eV}$  for Ru  $3d_{3/2}$  (Fig. 2b) [39]. To prevent the overlapping between Ru 3d and C 1s, the isolated Ru  $3p_{3/2}$  spectrum presents two main peaks at  $462.2$  and  $466.4 \text{ eV}$  (Fig. S7b), which is well recognized as the metallic Ru (0) and cationic Ru (IV) species, respectively, in which the metallic Ru (0) is dominated in the WR sample. Furthermore, the WR sample shows the highest proportion of Ru (0) among the samples (Figs. S7–S10, Table S4). After Ru loading, the electronic structure of O does not change significantly and  $\text{WO}_{2.72}$  acts as an electron provider, indicating that electrons transfer from the tungsten oxide substrate to the Ru species.

The atomic structure of WR catalyst is further elucidated by X-ray absorption spectra (XAS). Fig. 2c shows the normalized X-ray absorption near edge structure (XANES) spectra of W  $L_{3\text{-edge}}$  region of WR, and W foil and  $\text{WO}_3$  are used as the references. The absorption edge of the WR is higher than that of reference W and lower than  $\text{WO}_3$ , suggesting that the approximate W (VI) valence of WR. Compared with W foil and  $\text{WO}_3$ , the peak intensity of WR increases significantly as the central W atom site becomes more non-centrosymmetric, further indicating the presence of oxygen vacancies next to W atoms [38]. The W-O and W-W bonds are examined by the extended X-ray absorption fine structure (EXAFS) technique (Fig. 2d). The peak at  $1.4 \text{ \AA}$  is associated with the electronic back scatterings between W and neighboring O atoms in the first shell layer, while those at  $\sim 2.6 \text{ \AA}$  arise from the back scatterings of W-W. The spectrum of WR consists mainly of a stronger peak at  $1.4 \text{ \AA}$  belonging to the W-O bond, further confirming the main structure of  $\text{WO}_{2.72}$  in WR [40]. Photoluminescence (PL) spectroscopy and ultraviolet photoelectron spectroscopy (UPS) are adopted to investigate the interface electronic structure of WR [31,41]. In the PL spectrum (Fig. 2e), a blue-shifted emission peak is observed in WR Schottky composites, indicating a broadened band gap in WR caused by the band change. Moreover, the decreased intensity of PL quenching suggests that the recombination of electron-hole pair in WR composites is suppressed, resulting in the promoted charge separation, which would benefit the continued electron transportation in HER [32]. According to the band theory of solids physics [42], the state of electron transfer is closely related to the work function of specific materials. The work function of  $\text{WO}_{2.72}$  is calculated to be  $4.2 \text{ eV}$  through the UPS spectrum (Fig. 2f), and that of Ru is  $4.7 \text{ eV}$  according to the metal work function table, meaning that  $\text{WO}_{2.72}$  and Ru can readily form a Mott-Schottky barrier between each other, offering a potential of  $0.5 \text{ eV}$  to direct the charge transfer across the interface from  $\text{WO}_{2.72}$  to Ru [22,43,44]. Moreover,

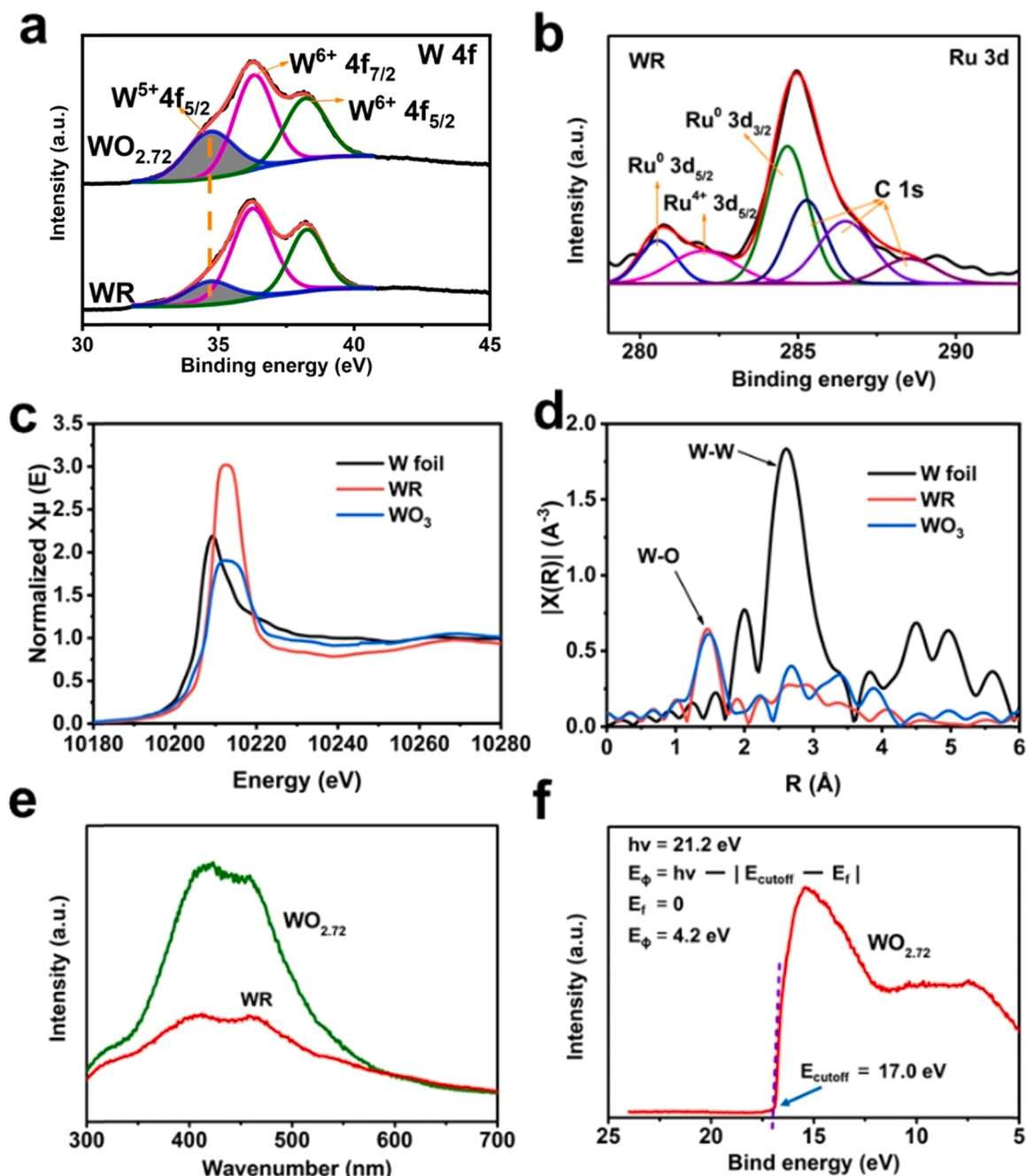


**Fig. 2.** (a) W 4f, and (b) Ru 3d XPS spectra of WR and WO<sub>2.72</sub>. (c) W L<sub>3</sub>-edge XANES spectra, and (d) Fourier-transformed EXAFS spectra for W foil, WR and WO<sub>3</sub>. (e) PL spectra of WO<sub>2.72</sub> and WR, (f) UPS profile of WO<sub>2.72</sub>.

the facile electron transfer can be further proved by MS plots (Fig. S12) [45,46]. WO<sub>2.72</sub> and WR are typical n-type semi-conductors, which possess a distinct positive slope in the MS plots. The flat band potential of WO<sub>2.72</sub> is 0.41 V, which is closed to the previous report [45,47]. A positive shift of flat band potential and lower slope were observed after loading of Ru (WR, 0.48 V), which is benefit for H<sup>+</sup> adsorption and electron transfer [48].

### 3.2. Electrocatalytic HER performance

The electrocatalytic activity is evaluated by linear sweep voltammetry (LSV) technique in the acid electrolyte using a typical three-electrode system. The pristine WO<sub>2.72</sub> sample exhibits a low electrocatalytic activity, it requires an overpotential of 320 mV to reach

10 mA cm<sup>-2</sup> current density in 0.5 M H<sub>2</sub>SO<sub>4</sub> (Fig. 3a). While the as-obtained WR shows significantly enhanced electrocatalytic activity for HER. Specifically, WR composite with a Ru loading amount of 2.73 wt% shows an extremely low onset potential of 10 mV and an overpotential of 40 mV to afford 10 mA cm<sup>-2</sup> (Fig. 3a), which is significantly lower than that of commercial Ru/C and highly comparable with state-of-art commercial Pt/C (Fig. 3b). Such high catalytic activity of WR is comparable to and even higher than those of the reported Ru-based composites with higher Ru loading amounts (Table S5). While WR3 sample exhibits relatively poor performance (Fig. S13a), mainly due to the much shorter nanowires of urchin-like morphology leading to the decrease of active sites exposure (Fig. S5) and the low proportion of Ru (0) (Table S4). A much lower Tafel slope of 50 mV dec<sup>-1</sup> of WR indicates greatly promoted HER kinetics, following a classical Volmer-Heyrovsky

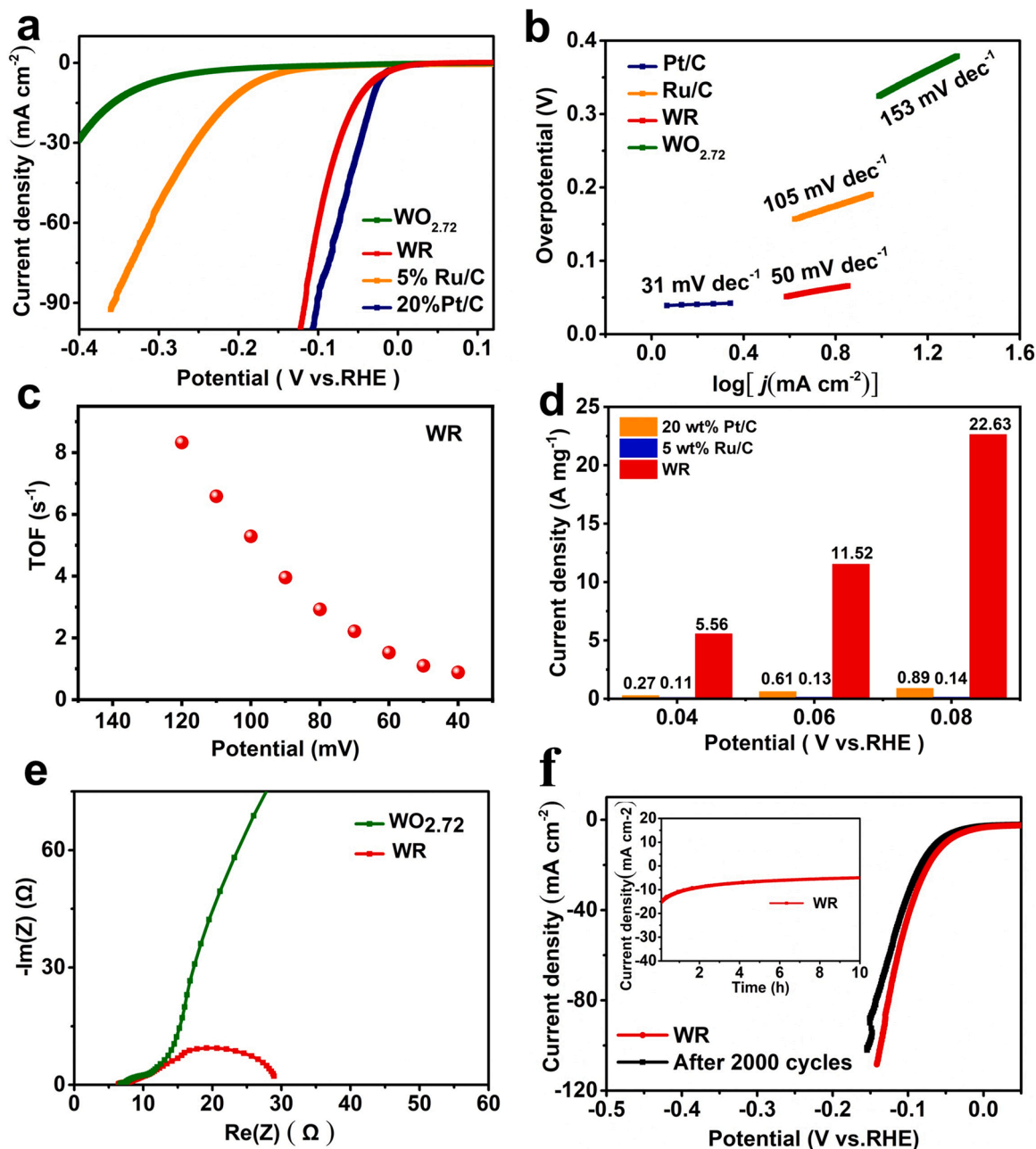


**Fig. 3.** (a) LSV curves and (b) Tafel slopes of  $\text{WO}_{2.72}$ , WR (2.73 wt% Ru), Ru/C (5 wt% Ru) and Pt/C (20 wt% Pt). (c) TOF values at different overpotentials of WR. (d) Mass activity histograms of WR, Ru/C and Pt/C. (e) EIS spectra of WR and  $\text{WO}_{2.72}$ . and (f) LSV curves of WR before and after 2000 cycles (inset: stability test of WR at 50 mV).

pathway (Fig. 3b) [49,50]. The calculated electrochemical surface areas (ECSA) of WR and  $\text{WO}_{2.72}$  are  $1147.56 \text{ cm}^2$  and  $495.14 \text{ cm}^2$ , respectively from their corresponding double layer capacitances ( $C_{dl}$ ) of  $91.63$  and  $39.49 \text{ mF cm}^{-2}$  (Fig. S14). A higher exchange current density ( $j_0$ ) of  $0.96 \text{ mA cm}^{-2}$  and turnover frequency (TOF) of  $5.29 \text{ s}^{-1}$  at the overpotential of  $100 \text{ mV}$  further suggest its high intrinsic activity of WR (Fig. 3c) [50,51]. The normalized mass activity of WR composite based on the Ru loading amount is remarkably 18.89–25.43 times and 161.6–50.5 times higher than Pt/C (20 wt%) and Ru/C (5 wt%), respectively (Fig. 3d), indicating an extraordinarily high atom-utilization ratio of WR [50]. Moreover, electrochemical impedance spectroscopy (EIS) shows that the resistance ( $R_c$ ) of WR is largely reduced, suggesting the enhanced electron transfer rates at the reaction surface/interface between electrolyte and catalysts (Fig. 3e) [15,52]. The relationship between the theoretical electrochemical result and

actual generated  $\text{H}_2$  amount is shown in Fig. S15, and the measured  $\text{H}_2$  amount agrees well with the calculated value with a high Faradic efficiency of 96.4% for  $\text{H}_2$  evolution.

WR also delivers an excellent electrochemical stability (Fig. 3f), a slight change is found even after 2000 cycles, and the current density can be maintained over 90% for 10 h (Fig. 3f inset) and over 80% for 24 h (Fig. S16) continuous operation. As a comparison, the current density of 20 wt% Pt/C can be maintained just 30% for 10 h continuous operation (Fig. S17). SEM, TEM and XPS characterizations of WR after 24 h electrochemical test have also been carried out. It is obvious that the nanowires of WR disappeared and the morphology of urchin-like nanospheres was changed (Fig. S18), indicating the decrease of active sites exposure resultantly the performance degradation. Moreover, a change of W valence has been observed (Fig. S19), in which W(V) almost all transformed into W(VI). Meanwhile, the proportion of  $\text{Ru}^{4+}$  also has



a positive shift, suggesting WR was oxidized at some degree during the durability test, which results in a drop in HER performance to some extent.

### 3.3. DFT calculation

Density functional theory (DFT) calculations are carried out to gain insights into the electronic and transfer properties of WR heterojunctions. The work function is calculated here as the energy difference between electrostatic potential and the Fermi level. The work function of the WO<sub>2.72</sub> (010) and Ru (1–10) surfaces is 4.02 and 4.78 eV (Fig. 4a and b), respectively, suggesting that the Fermi level of Ru (1–10) is significantly lower than that of WO<sub>2.72</sub>. Since Ru is decorated on the WO<sub>2.72</sub> surface, the electrons will transfer from WO<sub>2.72</sub> to Ru until the two Fermi energies are aligned. As shown in Fig. 4c, the work function of WR is 3.44 eV, indicating an enhanced capability for offering electrons from the negatively charged Ru sites. The difference in charge density reveals a strong charge redistribution after the addition of Ru (Fig. 4g). It can promote a significant increase in the internal electron concentration of the system, thus enhancing the H<sup>+</sup> adsorption and HER performance. Moreover, based on the charge density distributions of WO<sub>2.72</sub> and WR,

the electron density of states (DOS) at the Fermi level is significantly increased by Ru decoration (Fig. 4d), manifesting the electron transfer between the components, i.e., electron redistribution within the WR composite. The comparison between the partial DOS (PDOS) of the WO<sub>2.72</sub> and WR reveals that the enhanced DOS of the WR near the Fermi level is mainly contributed by the Ru d orbitals (Fig. 4e and f), indicating that the Ru species is responsible for the  $\pi$ -electron donation near the Fermi level, thus leading to the enhanced HER activity. Moreover, the  $\Delta G_{H^*}$  was calculated as a key factor of the HER activity (Fig. 4h), appropriate  $\Delta G_{H^*}$  can greatly improve the efficiency of HER reaction. According to the calculation, H adsorption is more likely to occur on the oxygen atoms of WO<sub>2.72</sub>, and the  $\Delta G_{H^*}$  values of WR (−0.33 eV) is approximately close to zero compared to those on WO<sub>2.72</sub> (−0.78 eV), resulting in a more preferable H<sup>+</sup> adsorption/desorption on WR.

### 3.4. Mechanism discussion

Combined with the experimental analysis and DFT calculations, we then discuss the Mott-Schottky effect and HER mechanism in the WR electrocatalyst (Fig. 4i, Fig. S20). Due to a lower work function of WO<sub>2.72</sub> than that of Ru, the conduction band edge of WO<sub>2.72</sub> would be

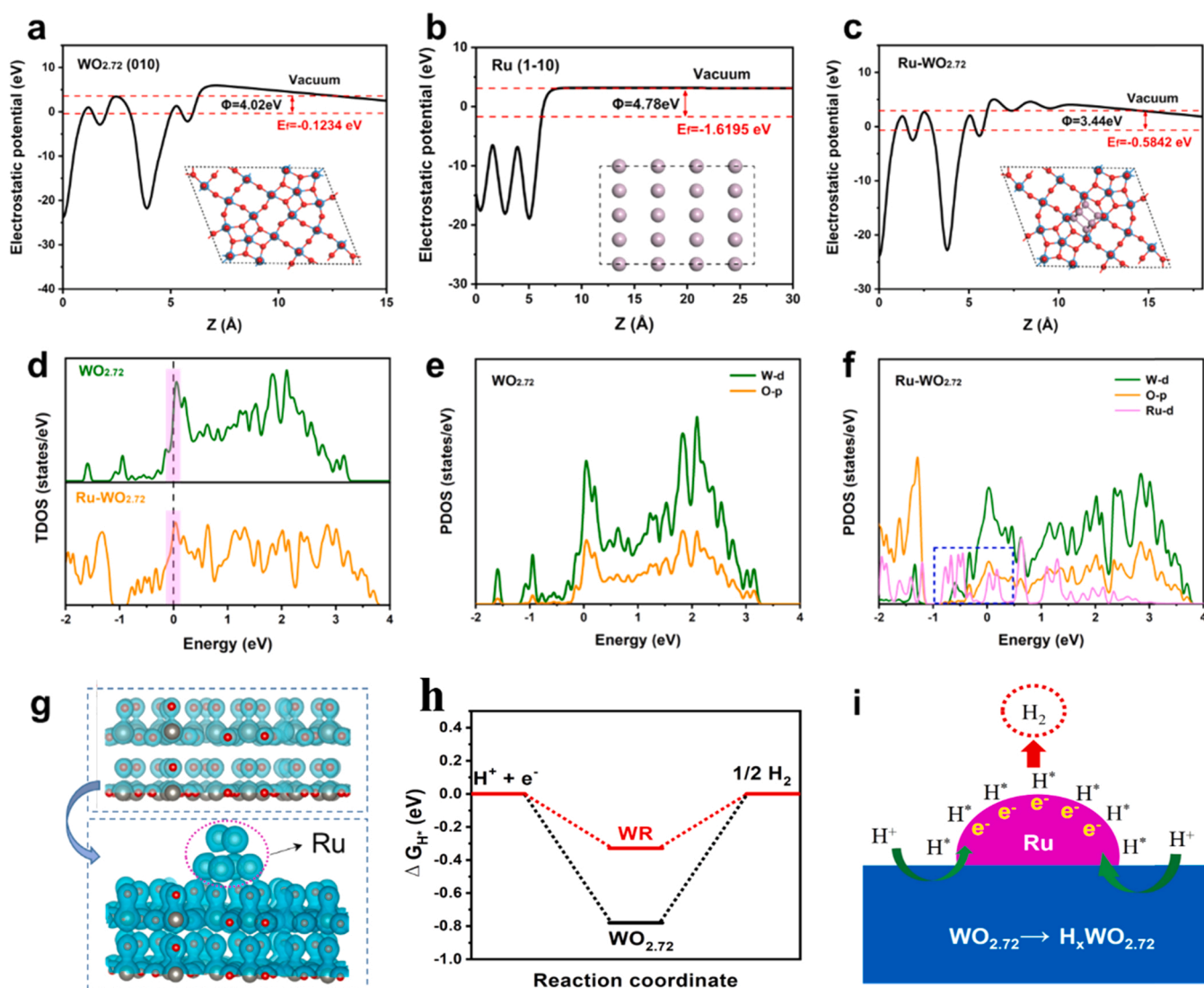
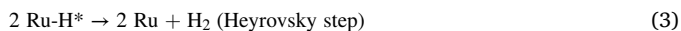
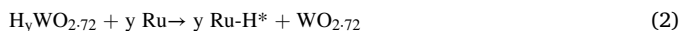
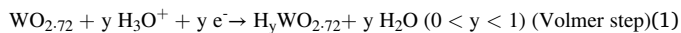


**Fig. 4.** Electrostatic potentials on the surfaces of WO<sub>2.72</sub> (010) plane (a), Ru (1–10) plane (b) and WR (c) by work functions. (d) Calculated DOS of WO<sub>2.72</sub> and WR. (e) PDOS of WO<sub>2.72</sub>. (f) PDOS of WR. (g) Calculated charge density difference of WO<sub>2.72</sub> (up) and WR (down). (h) Free energy diagram on WR and WO<sub>2.72</sub> (010) plane; (i) Schematic model of the HER mechanism of WR ( $E_{vac}$  = vacuum energy,  $E_c$  = conduction band,  $E_v$  = valence band,  $E_f$  = Fermi level).

upshifted after the introduction of Ru. The free electrons will spontaneously transfer from  $\text{WO}_{2.72}$  to Ru until the Fermi levels are aligned, which would induce an interfacial electric field [53]. Consequently, the charge redistribution of Ru and  $\text{WO}_{2.72}$  would endow an electron-rich region on the Ru surface and enhance the binding capability with protons. In addition,  $\text{WO}_3$  is a kind of typical material and can form a hydrogen tungsten bronze compound ( $\text{H}_y\text{WO}_3$ ) in acidic electrolyte through H insert/insert out realizing the hydrogen transfer from the active site to  $\text{WO}_3$  substrate [23,24]. Therefore, the HER process is speculated as follows:



The whole HER process is accelerated by the Mott-Schottky structure via the efficient electron distribution regulation and the phase transition between  $\text{WO}_{2.72}$  and  $\text{H}_y\text{WO}_{2.72}$ , respectively (Fig. 4i). Specifically,  $\text{WO}_{2.72}$  participates acts as a carrier which is easily to adsorb  $\text{H}^+$  to form a hydrogen tungsten bronze compound ( $\text{H}_y\text{WO}_3$ ) in acidic electrolyte (Volmer step). Then, the electron enrichment on the surface of Ru leads  $\text{H}^*$  to transfer to the surface of Ru (step 2). Eventually, hydrogen molecule formation occurs on the surface of Ru (Heyrovsky step). Benefiting from the synergistic effect between Ru and  $\text{WO}_{2.72}$  in the Mott-Schottky heterojunction effect, the kinetics of HER is thus significantly enhanced.

#### 4. Conclusion

In summary, we report a facile construction of WR Mott-Schottky heterojunction for efficient hydrogen evolution. The resultant WR composite with a low amount Ru loading (2.73 wt%) exhibits an excellent HER activity, featuring a low overpotential of 40 mV at the current density of  $10 \text{ mA cm}^{-2}$ , and its Ru-based utilization ratio is 18.89–25.43 times and 50.5–161.6 times higher than those of commercial Pt/C (20%) and Ru/C (5%), respectively. The outstanding HER performance is attributed to the synergistic effect between Ru clusters and  $\text{WO}_{2.72}$  substrate. The interface coupling between  $\text{WO}_{2.72}$  and Ru creates Mott-Schottky barriers, which is responsible for the electron transport from  $\text{WO}_{2.72}$  to Ru, and the resultant electron-enriched Ru surface. This work demonstrates an insightful concept in design and fabrication of Mott-Schottky heterojunction electrocatalysts for highly efficient hydrogen production and other energy technologies.

#### CRedit authorship contribution statement

**Lingxin Peng:** Conceptualization, Validation, Formal analysis, Investigation, Writing – original draft. **Liang Su:** Conceptualization, Investigation, Formal analysis, Writing – original draft. **Xu Yu:** Conceptualization, Validation, Formal analysis, Investigation, Writing – original draft. **Rongyan Wang:** Methodology. **Xiangzhi Cui:** Conceptualization, Supervision, Writing – review & editing. **Han Tian:** Investigation. **Shaowen Cao:** Resources. **Bao Yu Xia:** Conceptualization, Resources, Writing – review & editing. **Jianlin Shi:** Conceptualization, Methodology, Supervision, Writing – review & editing.

#### Declaration of Competing Interest

The authors declare that they have no known competing financial interests or personal relationships that could have appeared to influence the work reported in this paper.

#### Acknowledgements

Lingxin Peng, Liang Su and Xu Yu contributed equally to this work.

The authors gratefully acknowledge the support of this research by National Natural Science Foundation of China (21835007, 5217021722), Natural Science Foundation of Shanghai (19ZR1479400), the “Scientific and Technical Innovation Action Plan” Hong Kong, Macao and Taiwan Science & Technology Cooperation Project of Shanghai Science and Technology Committee (21520760500), the State Key Laboratory of Advanced Technology for Materials Synthesis and Processing (Wuhan University of Technology) and The Innovation and Talent Recruitment Base of New Energy Chemistry and Device (B21003).

#### Appendix A. Supporting information

Supplementary data associated with this article can be found in the online version at doi:10.1016/j.apcatb.2022.121229.

#### References

- [1] S. Chu, A. Majumdar, Opportunities and challenges for a sustainable energy future, *Nature* 488 (2012) 294–303, <https://doi.org/10.1038/nature11475>.
- [2] Y. Jiao, Y. Zheng, M. Jaroniec, S.Z. Qiao, Design of electrocatalysts for oxygen- and hydrogen-involving energy conversion reactions, *Chem. Soc. Rev.* 44 (2015) 2060–2086, <https://doi.org/10.1039/c4cs00470a>.
- [3] J. Wang, W.H. Fang, Y. Hu, Y.H. Zhang, J.Q. Dang, Y. Wu, B.Z. Chen, H. Zhao, Z. X. Li, Single atom Ru doping 2H-MoS<sub>2</sub> as highly efficient hydrogen evolution reaction electrocatalyst in a wide pH range, *Appl. Catal. B-Environ.* 298 (2021), <https://doi.org/10.1016/j.apcatb.2021.120490>.
- [4] A. Le Goff, V. Artero, B. Jousset, P.D. Tran, N. Guillet, R. Metaye, A. Fihri, S. Palacin, M. Fontecave, From hydrogenases to noble metal-free catalytic nanomaterials for H<sub>2</sub> production and uptake, *Science* 326 (2009) 1384–1387, <https://doi.org/10.1126/science.1179773>.
- [5] H. Wu, C. Feng, L. Zhang, J. Zhang, D.P. Wilkinson, Non-noble metal electrocatalysts for the hydrogen evolution reaction in water electrolysis, *Electrochem. Energy Rev.* (2021), <https://doi.org/10.1007/s41918-020-00086-z>.
- [6] C.-T. Dinh, A. Jain, F.P.G. de Arquer, P. De Luna, J. Li, N. Wang, X. Zheng, J. Cai, B. Z. Gregory, O. Voznyy, B. Zhang, M. Liu, D. Sinton, E.J. Crumlin, E.H. Sargent, Multi-site electrocatalysts for hydrogen evolution in neutral media by destabilization of water molecules, *Nat. Energy* 4 (2018) 107–114, <https://doi.org/10.1038/s41560-018-0296-8>.
- [7] B. Sarkar, B.K. Barman, K.K. Nanda, Non-precious bimetallic CoCr nanostructures entrapped in bamboo-like nitrogen-doped graphene tube as a robust bifunctional electrocatalyst for total water splitting, *ACS Appl. Energy Mater.* 1 (2018) 1116–1126, <https://doi.org/10.1021/acsaem.7b00233>.
- [8] D. Voiry, R. Fullon, J. Yang, E.S.C. de Carvalho Castro, R. Kappera, I. Bozkurt, D. Kaplan, M.J. Lagos, P.E. Batson, G. Gupta, A.D. Mohite, L. Dong, D. Er, V. B. Shenoy, T. Asefa, M. Chhowalla, The role of electronic coupling between substrate and 2D MoS<sub>2</sub> nanosheets in electrocatalytic production of hydrogen, *Nat. Mater.* 15 (2016) 1003–1009, <https://doi.org/10.1038/nmat4660>.
- [9] J. Zhu, L. Hu, P. Zhao, L.Y.S. Lee, K.Y. Wong, Recent advances in electrocatalytic hydrogen evolution using nanoparticles, *Chem. Rev.* 120 (2020) 851–918, <https://doi.org/10.1021/acs.chemrev.9b00248>.
- [10] B.C. Liu, Y. Cheng, B. Cao, M.H. Hu, P. Jing, R. Gao, Y.P. Du, J. Zhang, J.H. Liu, Hybrid heterojunction of molybdenum disulfide/single cobalt atoms anchored nitrogen, sulfur-doped carbon nanotube/cobalt disulfide with multiple active sites for highly efficient hydrogen evolution, *Appl. Catal. B-Environ.* 298 (2021), <https://doi.org/10.1016/j.apcatb.2021.120630>.
- [11] X. Shi, K. Ueno, T. Oshikiri, Q. Sun, K. Sasaki, H. Misawa, Enhanced water splitting under modal strong coupling conditions, *Nat. Nanotechnol.* 13 (2018) 953–958, <https://doi.org/10.1038/s41565-018-0208-x>.
- [12] Y. Yang, M. Luo, W. Zhang, Y. Sun, X. Chen, S. Guo, Metal surface and interface energy electrocatalysis: fundamentals, performance engineering, and opportunities, *Chem* 4 (2018) 2054–2083, <https://doi.org/10.1016/j.chempr.2018.05.019>.
- [13] Y. Liu, C. Xiao, P. Huang, M. Cheng, Y. Xie, Regulating the charge and spin ordering of two-dimensional ultrathin solids for electrocatalytic water splitting, *Chem* 4 (2018) 1263–1283, <https://doi.org/10.1016/j.chempr.2018.02.006>.
- [14] Z. Chen, Y. Song, J. Cai, X. Zheng, D. Han, Y. Wu, Y. Zang, S. Niu, Y. Liu, J. Zhu, X. Liu, G. Wang, Tailoring the d-band centers enables Co<sub>4</sub>N nanosheets to be highly active for hydrogen evolution catalysis, *Angew. Chem. Int. Ed.* 57 (2018) 5076–5080, <https://doi.org/10.1002/anie.201801834>.
- [15] K. Xu, Y. Sun, Y. Zhang, G. Jia, Q. Zhang, L. Gu, S. Li, Y. Li, H.J. Fan, Yin-Yang harmony: metal and nonmetal dual-doping boosts electrocatalytic activity for alkaline hydrogen evolution, *ACS Energy Lett.* 3 (2018) 2750–2756, <https://doi.org/10.1021/acseenergylett.8b01893>.
- [16] S.L. Jiao, Z.Y. Yao, F. Xue, Y.F. Lu, M.C. Liu, H.Q. Deng, X.F. Ma, Z.X. Liu, C. Ma, H. W. Huang, S.C. Ruan, Y.J. Zeng, Defect-rich one-dimensional MoS<sub>2</sub> hierarchical architecture for efficient hydrogen evolution: coupling of multiple advantages into one catalyst, *Appl. Catal. B-Environ.* 258 (2019), <https://doi.org/10.1016/j.apcatb.2019.117964>.
- [17] C.Y. Jian, W.T. Hong, Q. Cai, J. Li, W. Liu, Surface electron state engineering enhanced hydrogen evolution of hierarchical molybdenum disulfide in acidic and



- alkaline media, *Appl. Catal. B-Environ.* 266 (2020), <https://doi.org/10.1016/j.apcatb.2020.118649>.
- [18] W. Peng, X.G. Li, Z.M. He, Z.S. Li, X.Y. Zhang, X.P. Sun, Q. Li, H. Yang, J.T. Han, Y. H. Huang, Electron density modulation of MoP by rare earth metal as highly efficient electrocatalysts for pH-universal hydrogen evolution reaction, *Appl. Catal. B-Environ.* 299 (2021), <https://doi.org/10.1016/j.apcatb.2021.120657>.
- [19] L. Zuo, R. Li, Y. Jin, T. Zhang, Homogeneous nanoporous Ni particles produced by dealloying Mg-based metallic glass as efficient hydrogen evolution electrocatalyst, *J. Electrochem. Soc.* 165 (2018) F207–F214, <https://doi.org/10.1149/2.1051803jes>.
- [20] J. Hou, Y. Sun, Y. Wu, S. Cao, L. Sun, Promoting active sites in core-shell nanowire array as Mott-Schottky electrocatalysts for efficient and stable overall water splitting, *Adv. Funct. Mater.* 28 (2018), 1704447, <https://doi.org/10.1002/adfm.201704447>.
- [21] X.H. Li, M. Antonietti, Metal nanoparticles at mesoporous N-doped carbons and carbon nitrides: functional Mott-Schottky heterojunctions for catalysis, *Chem. Soc. Rev.* 42 (2013) 6593–6604, <https://doi.org/10.1039/c3cs60067j>.
- [22] Y.-X. Liu, H.-H. Wang, T.-J. Zhao, B. Zhang, H. Su, Z.-H. Xue, X.-H. Li, J.-S. Chen, Schottky Barrier induced coupled interface of electron-rich N-doped carbon and electron-deficient Cu: in-built Lewis acid-base pairs for highly efficient CO<sub>2</sub> fixation, *J. Am. Chem. Soc.* 141 (2019) 38–41, <https://doi.org/10.1021/jacs.8b08267>.
- [23] J. Park, S. Lee, H.E. Kim, A. Cho, S. Kim, Y. Ye, J.W. Han, H. Lee, J.H. Jang, J. Lee, Investigation of the support effect in atomically dispersed Pt on WO<sub>3-x</sub> for utilization of Pt in the hydrogen evolution reaction, *Angew. Chem.* 131 (2019) 16184–16188, <https://doi.org/10.1002/ange.201908122>.
- [24] Y. Liu, M. Cheng, Z. He, B. Gu, C. Xiao, T. Zhou, Z. Guo, J. Liu, H. He, B. Ye, B. Pan, Y. Xie, Pothole-rich ultrathin WO<sub>3</sub> nanosheets that trigger N identical with N bond activation of nitrogen for direct nitrate photosynthesis, *Angew. Chem. Int. Ed.* 58 (2019) 731–735, <https://doi.org/10.1002/anie.201808177>.
- [25] B.K. Barman, B. Sarkar, P. Ghosh, M. Ghosh, G.M. Rao, K.K. Nanda, In situ decoration of ultrafine Ru nanocrystals on N-doped graphene tube and their applications as oxygen reduction and hydrogen evolution catalyst, *ACS Appl. Energy Mater.* 2 (2019) 7330, <https://doi.org/10.1021/acsami.9b01318>.
- [26] B.K. Barman, B. Sarkar, K.K. Nanda, Pd-coated Ru nanocrystals supported on N-doped graphene as HER and ORR electrocatalysts, *Chem. Commun.* 55 (2019) 13928–13931, <https://doi.org/10.1039/c9cc06208d>.
- [27] B. Sarkar, D. Das, K.K. Nanda, Construction of noble-metal alloys of cobalt confined N-doped carbon polyhedra toward efficient water splitting, *Green Chem.* 22 (2020) 7884–7895, <https://doi.org/10.1039/d0gc01736a>.
- [28] G.G. Kresse, J.J. Furthmüller, Efficient iterative schemes for Ab initio total-energy calculations using a plane-wave basis set, *Phys. Rev. B, Condens. Matter* 54 (1996) 11169, <https://doi.org/10.1103/PhysRevB.54.11169>.
- [29] G. Kresse, D. Joubert, From ultrasoft pseudopotentials to the projector augmented-wave method, *Phys. Rev. B* 59 (1999) 1758–1775, <https://doi.org/10.1103/PhysRevB.59.11169>.
- [30] J.P. Perdew, K. Burke, M. Ernzerhof, Generalized gradient approximation made simple, *Phys. Rev. Lett.* 77 (1996) 3865–3868, <https://doi.org/10.1103/PhysRevLett.77.3865>.
- [31] Y. Tian, S. Cong, W. Su, H. Chen, Q. Li, F. Geng, Z. Zhao, Synergy of W<sub>18</sub>O<sub>49</sub> and polyaniline for smart supercapacitor electrode integrated with energy level indicating functionality, *Nano Lett.* 14 (2014) 2150–2156, <https://doi.org/10.1021/nl5004448>.
- [32] Y. Lu, Y. Jiang, X. Gao, X. Wang, W. Chen, Strongly coupled Pd nanotetrahedron/tungsten oxide nanosheet hybrids with enhanced catalytic activity and stability as oxygen reduction electrocatalysts, *J. Am. Chem. Soc.* 136 (2014) 11687–11697, <https://doi.org/10.1021/ja5041094>.
- [33] Z.-F. Huang, J. Song, L. Pan, L. Wang, J.-J. Zou, Tungsten oxides for photocatalysis, electrochemistry, and phototherapy, *Adv. Mater.* 27 (2015) 5309–5327, <https://doi.org/10.1002/adma.201501217>.
- [34] F. Salleh, M.N.A. Tahari, A. Samsuri, T.S.T. Saharuddin, S.S. Sulhadi, M.A. Yarmo, Physical and chemical behaviour of tungsten oxide in the presence of nickel additive under hydrogen and carbon monoxide atmospheres, *Int. J. Hydrog. Energy* 46 (2021) 24814–24830, <https://doi.org/10.1016/j.ijhydene.2020.08.099>.
- [35] G. Xi, J. Ye, Q. Ma, N. Su, H. Bai, C. Wang, In situ growth of metal particles on 3D urchin-like WO<sub>3</sub> nanostructures, *J. Am. Chem. Soc.* 134 (2012) 6508–6511, <https://doi.org/10.1021/ja211638e>.
- [36] L. Sun, B. Wang, Y. Wang, High-temperature gas sensor based on novel Pt single atoms@SnO<sub>2</sub> nanorods@SiC nanosheets multi-heterojunctions, *ACS Appl. Mater. Interfaces* 12 (2020) 21808–21817, <https://doi.org/10.1021/acsami.0c02160>.
- [37] C. Chen, H. Tian, Z. Fu, X. Cui, F. Kong, G. Meng, Y. Chen, F. Qi, Z. Chang, L. Zhu, H. Huang, B.Y. Xia, J. Shi, Pt NPs-loaded siloxene nanosheets for hydrogen co-evolutions from Zn-H<sub>2</sub>O fuel cells-powered water-splitting, *Appl. Catal. B: Environ.* 304 (2022), <https://doi.org/10.1016/j.apcatb.2021.121008>.
- [38] H. Tian, X. Cui, L. Zeng, L. Su, Y. Song, J. Shi, Oxygen vacancy-assisted hydrogen evolution reaction of the Pt/WO<sub>3</sub> electrocatalyst, *J. Mater. Chem. A* 7 (2019) 6285–6293, <https://doi.org/10.1039/c8ta12219a>.
- [39] G. Chen, S. Desinan, R. Rosei, F. Rosei, D. Ma, Synthesis of Ni–Ru alloy nanoparticles and their high catalytic activity in dehydrogenation of ammonia borane, *Chem. Eur. J.* 18 (2012) 7925–7930, <https://doi.org/10.1002/chem.201200292>.
- [40] K. Ishisone, T. Isobe, S. Matsushita, M. Wakumura, T. Takei, A. Nakajima, Local structure investigation of WO<sub>x</sub> cluster modified on titanium-substituted hydroxyapatite for promoting charge separation under UV illumination, *J. Ceram. Soc. Jpn.* 128 (2020) 798–804, <https://doi.org/10.2109/jcersj2.20141>.
- [41] C. Rajkumar, B. Thirumalraj, S.M. Chen, P. Veerakumar, S.B. Liu, Ruthenium nanoparticles decorated tungsten oxide as a bifunctional catalyst for electrocatalytic and catalytic applications, *ACS Appl. Mater. Interfaces* 9 (2017) 31794–31805, <https://doi.org/10.1021/acsami.7b07645>.
- [42] M.R. Nellist, F.A. Laskowski, F. Lin, T.J. Mills, S.W. Boettcher, Semiconductor-electrocatalyst interfaces: theory, experiment, and applications in photoelectrochemical water splitting, *Acc. Chem. Res.* 49 (2016) 733–740, <https://doi.org/10.1021/acs.accounts.6b00001>.
- [43] L.-N. Zhang, Z.-L. Lang, Y.-H. Wang, H.-Q. Tan, H.-Y. Zang, Z.-H. Kang, Y.-G. Li, Cable-like Ru/WNO@C nanowires for simultaneous high-efficiency hydrogen evolution and low-energy consumption chlor-alkali electrolysis, *Energy Environ. Sci.* 12 (2019) 2569–2580, <https://doi.org/10.1039/c9ee01647c>.
- [44] H. Su, K.X. Zhang, B. Zhang, H.H. Wang, Q.Y. Yu, X.H. Li, M. Antonietti, J.S. Chen, Activating cobalt nanoparticles via the Mott-Schottky effect in nitrogen-rich carbon shells for base-free aerobic oxidation of alcohols to esters, *J. Am. Chem. Soc.* 139 (2017) 811–818, <https://doi.org/10.1021/jacs.6b10710>.
- [45] M.K. Mohanta, T.K. Sahu, D. Gogoi, N.R. Peela, M. Qureshi, Hexagonal boron nitride quantum dots as a superior hole extractor for efficient charge separation in WO<sub>3</sub>-based photoelectrochemical water oxidation, *ACS Appl. Energy Mater.* 2 (2019) 7457–7466, <https://doi.org/10.1021/acsami.9b01450>.
- [46] Z.H. Sun, Y.K. Wang, L.B. Zhang, H. Wu, Y.C. Jin, Y.H. Li, Y.C. Shi, T.X. Zhu, H. Mao, J.M. Liu, C.H. Xiao, S.J. Ding, Simultaneously realizing rapid electron transfer and mass transport in Jellyfish-like Mott-Schottky nanoreactors for oxygen reduction reaction, *Adv. Funct. Mater.* 30 (2020), <https://doi.org/10.1002/adfm.201910482>.
- [47] T. Zhang, Z. Zhu, H. Chen, Y. Bai, S. Xiao, X. Zheng, Q. Xue, S. Yang, Iron-doping-enhanced photoelectrochemical water splitting performance of nanostructured WO<sub>3</sub>: a combined experimental and theoretical study, *Nanoscale* 7 (2015) 2933–2940, <https://doi.org/10.1039/c4nr07024k>.
- [48] B. Sarkar, D. Das, K.K. Nanda, pH-dependent hydrogen evolution using spatially confined ruthenium on hollow N-doped carbon nanocages as a Mott-Schottky catalyst, *J. Mater. Chem. A* 9 (2021) 13958–13966, <https://doi.org/10.1039/d1ta02375f>.
- [49] Y. Zheng, Y. Jiao, A. Vasileff, S.Z. Qiao, The hydrogen evolution reaction in alkaline solution: from theory, single crystal models, to practical electrocatalysts, *Angew. Chem. Int. Ed.* 57 (2018) 7568–7579, <https://doi.org/10.1002/anie.201710556>.
- [50] S. Anantharaj, S.R. Ede, K. Karthick, S. Sam Sankar, K. Sangeetha, P.E. Karthik, S. Kundu, Precision and correctness in the evaluation of electrocatalytic water splitting: revisiting activity parameters with a critical assessment, *Energy Environ. Sci.* 11 (2018) 744–771, <https://doi.org/10.1039/c7ee03457a>.
- [51] S. Park, J. Park, H. Abroshan, L. Zhang, J.K. Kim, J. Zhang, J. Guo, S. Siahrostami, X. Zheng, Enhancing catalytic activity of MoS<sub>2</sub> basal plane S-vacancy by Co cluster addition, *ACS Energy Lett.* 3 (2018) 2685–2693, <https://doi.org/10.1021/acsenenergylett.8b01567>.
- [52] C. Lei, Y. Wang, Y. Hou, P. Liu, J. Yang, T. Zhang, X. Zhuang, M. Chen, B. Yang, L. Lei, C. Yuan, M. Qiu, X. Feng, Efficient alkaline hydrogen evolution on atomically dispersed Ni–N<sub>x</sub> species anchored porous carbon with embedded Ni nanoparticles by accelerating water dissociation kinetics, *Energy Environ. Sci.* 12 (2019) 149–156, <https://doi.org/10.1039/c8ee01841c>.
- [53] Z.-H. Xue, H. Su, Q.-Y. Yu, B. Zhang, H.-H. Wang, X.-H. Li, J.-S. Chen, Janus Co/CoP nanoparticles as efficient Mott-Schottky electrocatalysts for overall water splitting in wide pH range, *Adv. Energy Mater.* 7 (2017), <https://doi.org/10.1002/aenm.201602355>.